Hugoniot and release measurements in diamond shocked up to 26 Mbar

M. C. Gregor,[1,2] D. E. Fratanduono,[3] C. A. McCoy,[4] D. N. Polsin,[1,2] A. Sorce,[1] J. R. Rygg,[1,2,5] G. W. Collins,[1,2,5] T. Braun,[3] P. M. Celliers,[3] J. H. Eggert,[3] D. D. Meyerhofer,[6] and T. R. Boehly[1]

[1]*Laboratory for Laser Energetics, University of Rochester, Rochester, New York 14623, USA*
[2]*Department of Physics and Astronomy, University of Rochester, Rochester, New York 14627, USA*
[3]*Lawrence Livermore National Laboratory, Livermore, California 94550, USA*
[4]*Sandia National Laboratories, Albuquerque, New Mexico 87185-1195, USA*
[5]*Department of Mechanical Engineering, University of Rochester, Rochester, New York 14627, USA*
[6]*Los Alamos National Laboratory, Los Alamos, New Mexico 87545, USA*

(Received 2 December 2016; published 26 April 2017)

The equation of state (EOS) of carbon in its high-pressure solid and liquid phases is of interest to planetary astrophysics and inertial confinement fusion. Of particular interest are the high-pressure shock and release responses of diamond as these provide rigorous constraints on important paths through the EOS. This paper presents experimental Hugoniot and release data for both single-crystal diamond (SCD) and nanocrystalline diamond (NCD), which is comprised of nanometer-scale diamond grains and is ∼5% less dense than SCD. We find that NCD has a stiffer Hugoniot than SCD that can be attributed to porosity. A Grüneisen parameter of ∼1 was derived from the data, which suggests increased coordination in the high-pressure fluid carbon compared to ambient diamond.

DOI: 10.1103/PhysRevB.95.144114

I. INTRODUCTION

The behavior of carbon at millions to billions of atmospheres of pressure is integral to evolution models for many solar and extrasolar planets (Uranus, Neptune, 55 Cancri E) [1,2] and white dwarf stars [3,4]. In Uranus and Neptune, carbon exists in the form of methane (CH_4) ice at the surface but may be in its elemental form near the core where pressures and temperatures reach ∼8 Mbar and ∼8000 K, respectively [5,6]. Theoretical predictions suggest that the interiors of Uranus, Neptune, or Neptune-like exoplanets might contain diamond or even liquid oceans of carbon [1,5]. This strongly motivates studies of carbon's high-pressure response in both its solid and liquid phases [7–9].

Carbon's equation of state (EOS) is important to developing predictive models for inertial confinement fusion (ICF) experiments, where diamond shells are used to contain and compress the hydrogen fuel [10,11]. An ICF implosion uses a series of finely tuned shock waves to precompress the shell (ablator) and fuel. This initiates nearly isentropic compression while adding the desired amount of entropy needed to hydrodynamically stabilize the main implosion. An optimal target design is a delicate balance between these two effects. The diamond used in ICF targets is polycrystalline with grain sizes of ∼10 nm [12,13]. The low surface roughness and isotropic character of this nanocrystalline diamond (NCD) compared to single-crystal diamond (SCD) makes NCD less susceptible to hydrodynamic instabilities seeded by crystal anisotropy at the ablator/fuel interface. Current implosion designs melt the NCD with the first shock to further limit instability growth. Modeling an ICF implosion requires accurate knowledge of NCD's response to multimegabar shocks and its behavior when it releases from these extreme pressures into the low-density fuel.

To date, data for carbon above the diamond melt boundary are limited to shock compression measurements [14–16]. None of these data include NCD; high-precision measurements (relative density error <1.5%) for SCD exist up to only 19 Mbar [14]. Shock Hugoniot data in solid diamond [17–19] and the solid–liquid coexistence region [7,8,14] are supplemented by ramp-compression measurements [20,21], which are used to explore matter at temperatures significantly lower than temperatures on the Hugoniot. Ramp-compression data exist up to 8 Mbar for solid full-density diamond [21] and 50 Mbar for solid lower-density NCD [20] but theories describing liquid carbon above 19 Mbar are unconstrained by high-precision experiments. The experiments presented here provide high-pressure (up to 26 Mbar) shock-compression and release data for both full-density SCD ($\rho_0 = 3.515$ g cm^{-3}) and the lower-density NCD ($\rho_0 \sim 3.36$ g cm^{-3}) used in ICF capsules. The Hugoniot data provide a clear constraint on the pressure, density, and internal energy of liquid carbon, while the release data constrain the isentropes from these high-pressure, high-temperature shock states to a several-fold drop in pressure [22,23].

Single-shock Hugoniot data for diamond (both SCD and NCD) were collected up to 26 Mbar [∼60 000 K (Ref. [7])] using impedance-matching (IM) techniques with quartz as a reference material. These new SCD Hugoniot data agree with density-functional theory molecular dynamics (DFT-MD) calculations for liquid carbon [24]. The data for NCD, which are expected to be at a slightly higher temperature, exhibit a compressibility that is even stiffer than shock-compressed SCD measurements and DFT-MD predictions. The NCD data suggest that either its thermal properties are inadequately understood or the shock compression of NCD undergoes an additional (frictional) heating related to its slightly lower density.

The release data were collected by releasing shock-compressed diamond into several lower-impedance materials with known shock Hugoniots: quartz [25,26], CH [27], silica foam [26,28], and liquid D_2 [29,30]. This technique was previously used by Knudson, Desjarlais, and Pribram-Jones

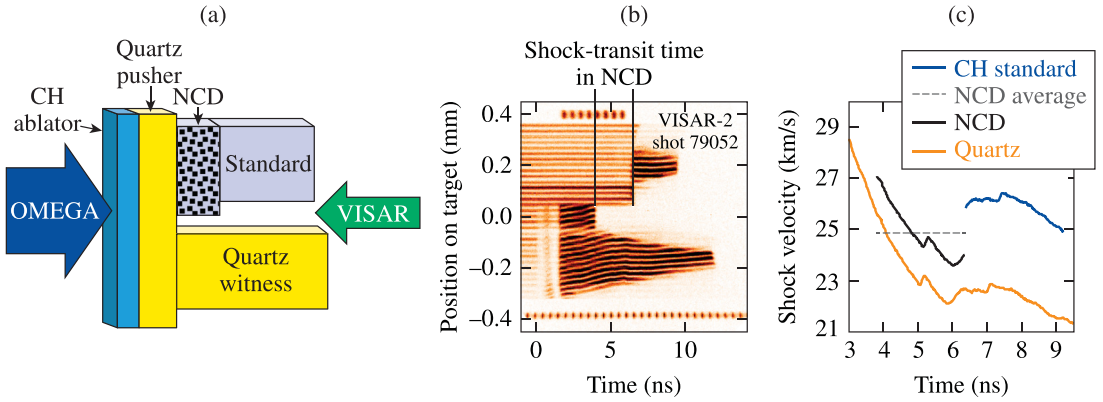

FIG. 1. (a) The nanocrystalline diamond (NCD) target design comprising a CH ablator, a quartz pusher and witness, an NCD sample, and a standard positioned to facilitate measurements of transit times. (b) Raw VISAR (velocity interferometer system for any reflector) data from an experiment using the target design in (a). (c) Extracted shock velocities from (b). The shock-velocity history in NCD (solid black) was inferred from the average shock velocity (dashed gray) and the observed shock-velocity history in the adjacent quartz witness (solid orange) using the nonsteady waves correction [36]. The shock-velocity profile in the CH standard (solid blue) is observed once the shock breaks out of the NCD.

to benchmark the release of shocked aluminum [30] and quartz [26]. Data were acquired for diamond releasing from 8 to 20 Mbar, so release paths originated from both the coexistence region and the liquid phase. The SCD release data mostly agree with predictions using existing EOS models that do not include strength effects, indicating that strength does not largely affect the diamond release physics at these pressures. The release measurements into the low-density liquid D_2 are particularly valuable for constraining ICF models since liquid D_2 is a good surrogate for the deuterium-tritium fuel in an ICF target [31,32].

Off-Hugoniot behavior in shock experiments is typically obtained using analytical models, which reference departures from the principal Hugoniot using thermodynamic derivatives such as the Grüneisen parameter (Γ). This work provides the first experimental measurement of Γ for liquid carbon at terapascal pressures, which is useful for constraining various models for high-pressure carbon. The Grüneisen parameter was determined using three independent analyses. The difference between the SCD and NCD Hugoniots was first used to extract Γ. This value of $\sim$1 was then confirmed using release data for both NCD and SCD.

The experimental design, targets, and diagnostics used in the laser-driven shock experiments are described in Sec. II. The IM technique used to measure Hugoniot and release states is described in Sec. III. The NCD data analysis techniques are described in Sec. IV followed by the results in Sec. V.

II. EXPERIMENTAL TECHNIQUE

The experiments were performed at the University of Rochester's Omega Laser Facility, a Nd:glass laser that is frequency tripled to a wavelength of 351 nm [33]. The experiments used 6 to 12 beams having temporally square pulses with durations of 2, 3, or 3.7 ns with total energies between 1.1 and 3.7 kJ. The beam profiles with an $\sim$876-μm-diameter laser focal spot were smoothed using spectral dispersion [34] and distributed phase plates [35]. On-target laser irradiances of 0.66 to 3.3 $\times$ 10^{14} W cm^{-2} were achieved, producing shock pressures up to 26 Mbar in the diamond targets.

The NCD targets were designed to provide both Hugoniot and release measurements on each shot. The targets [Fig. 1(a)] comprised a CH ablator, a Z-cut α-quartz standard (pusher), and an NCD sample glued to the pusher's rear surface. IM data were obtained at this interface for NCD Hugoniot measurements. A standard material [quartz, polystyrene (CH), SiO_2 foam, or liquid D_2] was in contact with the rear side of the NCD sample to determine its release behavior. Adjacent to the NCD sample, a quartz witness provided a reference for the temporal history of the shock velocity. The witness was required because internal scattering attributed to the nanometer-sized diamond grains and their random orientations make NCD translucent to visible light [13]. For this reason, shock velocities in the NCD were measured from transit times. To facilitate these measurements, the NCD sample and rear standard were positioned to provide an unobstructed view of $\sim$100 μm of the rear quartz pusher and NCD faces as shown in Figs. 1(a) and 1(b).

Examples of planar cryogenic and warm SCD target designs are shown in Fig. 2. SCD is transparent, obviating the need for the quartz witness. This allowed us to use one to three rear standards to obtain multiple release measurements on a single shot. Hugoniot measurements were made at the quartz/SCD interface and release measurements were made at the SCD/rear-standard interface. A thin (0.3- or 2-μm) gold layer was deposited on the rear of the CH ablator in some targets to help prevent preheat in the SCD and standards. A quartz baseplate (30 to 50 μm thick) was directly attached to the front side of the SCD whenever a gold layer was not used. The 0.3-μm gold layer was also used in some NCD targets.

The NCD targets used the same nanocrystalline diamond (fabricated by Diamond Materials GmbH) used in ICF targets at the National Ignition Facility (NIF) [37]. The density of the NCD samples was determined to be 3.360 $\pm$ 0.002 g cm^{-3} using an Archimedes' measurement of a larger reference sample from the same batch [13]. The SCD foils obtained from Applied Diamond had a density of $\rho_0 = 3.515$ g cm^{-3} and were natural with a $\langle 110 \rangle$ orientation or chemical vapor deposition (CVD) with a $\langle 100 \rangle$ orientation. The quartz

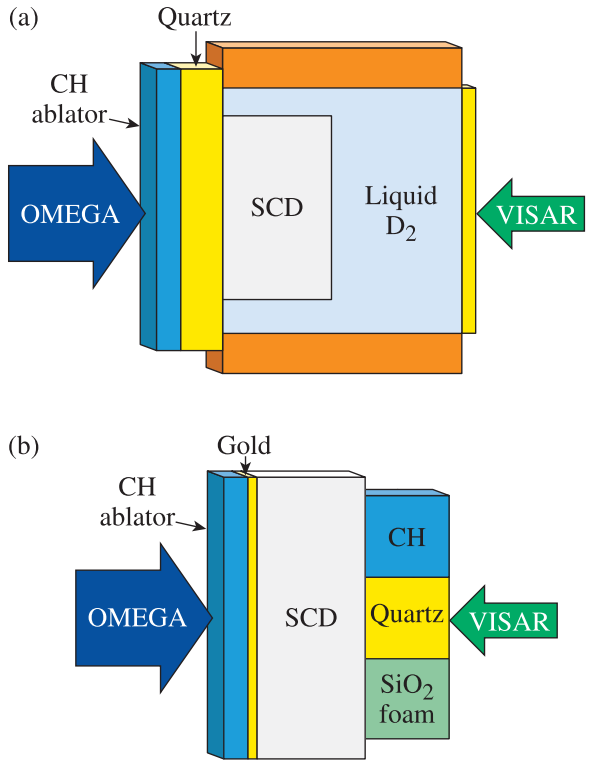

FIG. 2. Schematics of (a) planar cryogenic and (b) warm targets used in single-crystal (SCD) Hugoniot and release experiments. Targets had a CH ablator and one to three standards (liquid D_2, CH, quartz, or SiO_2 foam) on the rear side of the SCD.

($\rho_0 = 2.65\,\mathrm{g\,cm^{-3}}$), CH ($\rho_0 = 1.05\,\mathrm{g\,cm^{-3}}$), and SiO_2 foam ($\rho_0 \sim 0.2\,\mathrm{g\,cm^{-3}}$) (see Table II for exact values) pieces were obtained from Schafer Corporation. The planar cryogenic targets [Fig. 2(a)] comprised a liquid D_2-filled cylindrical copper cell sealed with quartz on both faces. The initial D_2 density was determined from the temperature in the cryogenic cell (~20 K) and varied between 0.170 and $0.174\,\mathrm{g\,cm^{-3}}$ on a shot-to-shot basis [38]. The uncertainty in the SiO_2 foam density was estimated to be ~2%, and uncertainties in the SCD, quartz, CH, and liquid D_2 densities were assumed to be negligible (including the effects of cryogenic temperatures).

The shock velocities for impedance matching were measured using the line-imaging velocity interferometer system for any reflector (VISAR) described in Ref. [39]. Opposite the drive beams, the VISAR probe beam is incident on the rear side of the target and the reflected signal is relayed to a pair of interferometers. A delay etalon is inserted into one leg of each interferometer so that changes in Doppler shifts of the reflected probe beam, corresponding to moving reflective interfaces, are registered as fringe shifts in the interference pattern. The fringe shifts are proportional to the velocity of the moving interface through the velocity per fringe (VPF), which depends inversely on the etalon thickness and the index of refraction of the target medium at the 532-nm probe wavelength. The indices of refraction for the target materials at 532 nm are 2.42 (SCD), 1.55 (quartz), 1.59 (CH), 1.04 (0.2-g cm^{-3} SiO_2 foam) [28], and 1.14 (0.174-g cm^{-3} liquid D_2) [29].

The two interferograms, which are recorded on separate streak cameras, provide time histories of the velocity of moving interfaces with ~30-ps resolution [39]. Fringe jumps or 2π phase ambiguities between the two records are resolved by using etalons of different thicknesses. The velocities presented here for the NCD Hugoniot and all release measurements are those measured using the more-sensitive VISAR leg. Measurements using the less-sensitive VISAR leg are presented for some SCD Hugoniot measurements because it provided better-resolved fringe shifts of the decaying shock at the quartz/SCD interface. Errors were estimated to be the larger of 5% of a fringe using the more-sensitive leg or the difference between the velocity from the more-sensitive leg and the weighted velocity average from both legs. An example of raw VISAR data and extracted shock velocities from an NCD experiment using the target design in Fig. 1(a) are shown in Figs. 1(b) and 1(c).

The targets were shock compressed to a metallic fluid state producing a reflective shock front. For transparent materials, high-precision, *in situ*, time-varying shock velocities were measured [39]. In opaque or translucent materials, the VISAR probe beam cannot reach the shock front within the target. Instead, VISAR registers the time that the shock breaks out of the material. For example, the shock transit time in the NCD sample is given by the time between the two vertical lines in Fig. 1(b). The first time is registered by the arrival of the shock at the rear of the quartz pusher and the second time is registered from its arrival at the rear NCD interface. A streaked optical pyrometer (SOP) [40] with ~5-ps temporal resolution provided additional measurements of shock transit times. Average velocities in NCD were corrected using the nonsteady waves model [36] discussed in Sec. IV C.

III. IMPEDANCE-MATCHING TECHNIQUE

Both Hugoniot and release states in diamond were measured using impedance matching. The IM technique closes the Rankine-Hugoniot equations [23] to solve for pressure (P), density (ρ), and specific internal energy (E) in a shock-compressed material. These equations

$$\rho = \frac{\rho_0 U_s}{(U_s - u_p)}, \tag{1}$$

$$P = P_0 + \rho_0 U_s u_p, \tag{2}$$

$$E = E_0 + \frac{1}{2}(P + P_0)\left(\frac{1}{\rho_0} - \frac{1}{\rho}\right), \tag{3}$$

describe the jump conditions across a shock front where U_s is the shock velocity, u_p is the particle velocity, and states upstream of the shock are characterized by the subscript 0 [23]. By measuring U_s and u_p, the kinematic EOS parameters P, ρ, and E can be determined. In these experiments, U_s is measured using VISAR and u_p is determined using the IM technique, which relies on the equilibration of P and u_p at the interface between the material of interest (diamond) and a material with a known EOS. This method for measuring the Hugoniot and release behavior of diamond is described in the following two sections.

A. Hugoniot measurements

The Hugoniot of an uncharacterized sample is measured with knowledge of the standard's EOS and the shock velocities about the standard/sample interface. In this work, the diamond Hugoniot data were measured using a quartz standard [25,26]. The pressure and particle velocity in the shocked quartz at the quartz pusher/diamond interface is given by the intersection of the Rayleigh line [Eq. (2)] and the quartz Hugoniot (cubic form taken from Ref. [26]). When the shock crosses into the diamond, the pressure and particle velocity must be continuous at the contact interface to maintain equilibrium. Since diamond has higher impedance ($\rho_0 U_s$), the quartz is reshocked to a higher pressure, off its principal Hugoniot, to reach this new (P,u_p) state. This state, given by the intersection in the $P - u_p$ plane of the quartz reshock and the diamond Rayleigh line, marks a state on the diamond's Hugoniot.

The quartz reshock was modeled using a Mie-Grüneisen EOS [41] of the form

$$P = P_H + \Gamma\rho(E - E_H) \tag{4}$$

with

$$E - E_H = \frac{1}{2}(P + P_H)\left(\frac{1}{\rho_1} - \frac{1}{\rho}\right), \tag{5}$$

where P_H and E_H are the pressure and specific internal energy, respectively, on the quartz principal Hugoniot, ρ_1 is the density in the singly-shocked quartz upstream of the reshock, and ρ, P, and E are the density, pressure and specific internal energy, respectively, in the reshocked quartz. This reshock model used the same reference Hugoniot P_H and effective Grüneisen parameter $\Gamma = \Gamma_{eff}$ as the quartz release model described in Ref. [26]. It should be noted that P_H and Γ_{eff} are not necessarily physical; they were optimized such that the quartz release model matched experimental data and first-principles molecular dynamics simulations. This same construct should be accurate for modeling the reshock since the quartz compresses only 20% to 30%. The diamond $P - u_p$ data determined by this model are only 1% to 2% higher than those obtained using the simple reflected-Hugoniot approximation.

B. Release measurements

The release behavior of shocked diamond was measured by impedance matching between diamond and several lower-impedance standards. The initial and final states of the diamond release are determined using the known Hugoniots of the diamond materials (measured previously or in this study) and those of the standards. By using various lower-impedance standards, the diamond release is measured at incrementally lower end-state pressures, mapping the release path in $P - u_p$ space.

The release standards used in these experiments have been suitably characterized: quartz [25,26], CH [27], SiO_2 foam [26,28], and liquid D_2 [29,30]. Table I lists the coefficients for the fits to the $U_s - u_p$ data for each of the standards used in the release analysis.

The CH and liquid-D_2 Hugoniot fits used in this work were re-analyzed using new data for the standards used in those IM studies. The CH Hugoniot data from Barrios *et al.* [27], which used a quartz standard, were reanalyzed using the updated quartz Hugoniot and release model from Knudson and Desjarlais [26]. The liquid-D_2 Hugoniot data from Hicks *et al.* [29], which used an aluminum standard, were re-analyzed by Knudson, Desjarlais, and Pribram-Jones and presented in Ref. [30]. This liquid-D_2 Hugoniot was used in this analysis because both works were performed on the OMEGA laser and had the same initial liquid-D_2 densities to within 2.5%. Because the Hicks *et al.* Hugoniot fit was determined for $\rho_0^{Hicks} = 0.174$ g cm^{-3}, the $U_s^{D_2}$ data plotted in Sec. V C were normalized to that initial density using the corrective term $2.29(1 - \rho_0/\rho_0^{Hicks})$. This offset was determined in Ref. [29] by comparing the effect of ρ_0 on the Hugoniots modeled using the stiffest and softest D_2 EOS tables; it affected this data set by only <0.2%.

TABLE I. Weighted fits to the $U_s - u_p$ data for the standards used in the release analysis. Coefficients to the form $U_s = a + bu_p - cu_p e^{-du_p}$ are listed below. The coefficients for the quartz and silica foam fits were taken directly from Ref. [26]

Standard	a (km s^{-1})	b	c	d (km s^{-1})$^{-1}$
Quartz	6.278	1.193	2.505	0.3701
CH	2.697	1.332	0	0
Foam	− 0.389	1.248	0	0
Liquid D_2	2.694	1.179	0	0

Shock velocities in diamond and the standards were measured at the IM interface and are presented in Table II. The shock velocity in diamond at the point of breakout into the standard was measured directly from the VISAR data for SCD and inferred from the nonsteady waves correction for NCD. The shock velocity in the standard was extrapolated backward across the glue layer to this same point. The extrapolation was done by linearly fitting to the measured shock velocity over a 150- to 500-ps time interval when the shock first entered the standard. *HYDRA* [42] simulations for a different shock experiment involving a quartz/LiH interface with a 0-, 2-, and 4-μm-thick oil layer between them showed that extrapolating the shock velocity backward across the entire oil (or glue) layer (as opposed to midway) most accurately represented shock behavior at the interface when the two materials were in direct contact [43]. Only data with steady or smoothly decaying shocks over 150 ps on both sides of the interface were used in the release analysis.

In Sec. V C, the release data are compared to predictions using diamond EOS tables and Mie-Grüneisen EOS models. The Mie-Grüneisen release model has the same form as Eq.(4) but now P and E are the pressure and specific internal energy along the release isentrope, which are related through $dE = -PdV$, where V is the specific volume $(1/\rho)$. P as a function of only V is obtained by solving the differential equation for E:

$$P(V) = -\frac{dE}{dV} = P_H(V)\left[1 + \frac{\Gamma}{2}\left(\frac{V_0}{V} - 1\right)\right] + \frac{\Gamma}{V}E. \tag{6}$$

Equation (6) was obtained using the Rankine-Hugoniot relation [Eq. (3) with $P_0 = 0$ and $E = E - E_0$] in Eq. (4) [26].

TABLE II. Diamond release data. All the single-crystal diamond (SCD) samples were shock compressed along the ⟨110⟩ axis except for the SCD in shot 73733, which was compressed along the ⟨100⟩ axis. U_s^C and $U_s^{Stan.}$ are the shock velocities at the interface between the diamond and the lower-impedance standard (quartz, CH, SiO_2 foam, or liquid D_2). $U_s^{Stan.}$ was corrected to account for the glue layer (when necessary) by linearly fitting to the measured shock velocity in the standard over a 150- to 500-ps time interval and extrapolating the fit backward across the glue layer. The initial densities of the liquid D_2 and SiO_2 foam samples in mg cm^{-3} are listed in column 3.

Shot	Diamond type	Standard	U_s^C (km/s)	$U_s^{Stan.}$ (km/s)
77003	SCD	D_2 (174)	29.47 ± 0.06	38.60 ± 0.27
77848	SCD	D_2 (170)	28.56 ± 0.06	36.86 ± 0.12
77851	SCD	D_2 (170)	27.39 ± 0.09	34.49 ± 0.12
77856	SCD	D_2 (170)	29.10 ± 0.06	37.83 ± 0.13
79050	SCD	D_2 (174)	25.03 ± 0.10	30.14 ± 0.33
79053	SCD	D_2 (172)	24.62 ± 0.10	29.29 ± 0.22
73733	SCD	quartz	25.88 ± 0.06	24.52 ± 0.09
75397	SCD	quartz	23.67 ± 0.07	21.63 ± 0.15
75399	SCD	quartz	23.87 ± 0.07	21.92 ± 0.11
75400	SCD	quartz	23.20 ± 0.11	21.05 ± 0.16
75402	SCD	quartz	23.93 ± 0.07	21.77 ± 0.11
75404	SCD	quartz	29.05 ± 0.07	27.61 ± 0.11
77857	SCD	quartz	31.60 ± 0.06	30.17 ± 0.09
77859	SCD	quartz	31.57 ± 0.06	30.05 ± 0.09
77860	SCD	quartz	29.33 ± 0.06	28.29 ± 0.09
75397	SCD	CH	23.48 ± 0.07	24.00 ± 0.10
75399	SCD	CH	23.84 ± 0.13	24.94 ± 0.12
75400	SCD	CH	23.20 ± 0.07	23.36 ± 0.15
75404	SCD	CH	28.77 ± 0.07	32.00 ± 0.11
77857	SCD	CH	31.64 ± 0.06	35.37 ± 0.09
77859	SCD	CH	31.46 ± 0.06	35.08 ± 0.10
77860	SCD	CH	29.21 ± 0.06	32.46 ± 0.09
75397	SCD	foam (191)	23.63 ± 0.07	25.01 ± 0.16
75400	SCD	foam (191)	23.10 ± 0.07	24.51 ± 0.16
77004	NCD	D_2 (173)	26.69 ± 0.95	33.29 ± 0.12
77006	NCD	D_2 (172)	30.81 ± 0.80	40.20 ± 0.12
77002	NCD	quartz	31.22 ± 0.53	30.10 ± 0.09
77007	NCD	quartz	28.09 ± 0.36	26.48 ± 0.09
79048	NCD	quartz	22.16 ± 0.18	20.44 ± 0.16
77005	NCD	CH	28.09 ± 0.36	31.89 ± 0.09
77861	NCD	CH	25.76 ± 0.35	27.79 ± 0.09
77862	NCD	CH	24.48 ± 0.26	26.17 ± 0.09
79052	NCD	CH	23.94 ± 0.15	25.87 ± 0.16
79056	NCD	CH	26.57 ± 0.28	28.93 ± 0.16
79060	NCD	CH	22.92 ± 0.20	24.87 ± 0.25
79051	NCD	foam (198)	23.51 ± 0.25	26.22 ± 0.24

The Reimann integral written as a function of volume,

$$u_p = u_{p1} + \int_{V_1}^{V} \sqrt{\frac{-dP}{dV'}}\, dV', \tag{7}$$

is used to solve for the particle velocity along the release isentrope, where u_{p1} is the particle velocity on the Hugoniot from which the release path originates. This analytical release model relies only on the reference Hugoniot $[P_H(V)]$ and Γ, both of which are presented in Sec. V A.

IV. NCD DATA ANALYSIS

EOS data obtained from impedance matching require accurate measurements of shock velocities and error propagation to provide high-confidence data. Modern VISAR systems can provide <1% velocity measurements in transparent samples [39], yielding precise EOS data [27]. Opaque or translucent samples like NCD present a different challenge. The methods used to obtain average shock velocities (i.e., transit times) and to correct those velocities for unsteadiness are described below. The NCD transit time data and Hugoniot data are listed in Table III.

A. Measurements of shock transit times

Average shock velocities in the NCD samples were determined using the measured thicknesses and shock transit times. The VISAR and SOP were used to measure the times that the shock exited the quartz pusher (t_1) and the NCD (t_2). This defined the total time ($\Delta t_{total} = t_2 - t_1$) that the shock spent in the NCD sample and the glue layer preceding it. The transit time across the NCD sample alone is calculated by $\Delta t_{NCD} = \Delta t_{total} - \Delta x_{glue}/U_s^{glue}$, where Δx_{glue} is the estimated glue thickness (described in Sec. IV B) and U_s^{glue} is the shock velocity in the glue estimated using the *SESAME* 7603 table for epoxy and the known pressure and particle velocity at the quartz pusher/glue interface. On average, the glue correction decreased the average shock velocity in NCD by only 0.1%.

For targets with an uncovered NCD step, as shown in Fig. 1(a), shock breakout times were measured using the drop in the VISAR reflectivity across the step/vacuum interface seen in Fig. 1(b). The peak in the derivative of the reflectivity, denoting the steepest slope in the drop in signal, defined the shock breakout time. This method yielded the most-consistent and most-precise transit times since the peaks were measured to ~5 ps.

For targets without the steps, breakout times were defined by the rapid change in thermal emission recorded by the SOP at the quartz pusher/glue/witness interface (t_1) and the NCD/glue/standard interface (t_2). The steepest slope of the SOP signal was used to define t_1 and t_2. An additional uncertainty up to 50 ps was applied to these measurements because the location of the peak defining t_1 or t_2 varied with glue-layer thickness. This is because the SOP signal does not drop to zero at the glue (or liquid D_2) interface, as was observed in the VISAR reflectivity at the step/vacuum interface. As the shock approached the rear surface of the NCD sample, the VISAR reflectivity and the SOP signal increased exponentially because of reduced volumetric scattering. This contributed to the uncertainty in t_2 because the emission continuously increases across the NCD/glue/standard (or liquid D_2) interface.

B. Measurements of thickness

The step heights of the NCD samples glued to the quartz pushers (Δx_{total}) were measured using white-light interferometry with a Zygo NexView 3D optical surface profiler. The average NCD step height was referenced to the quartz pusher in the areas where the breakout times were measured. The glue thicknesses were estimated by

TABLE III. NCD transit time data and Hugoniot data from impedance matching (IM) with a quartz standard. The shock transit times (Δt_{total}) and thicknesses (Δx_{total} and Δx_{NCD}), where total denotes the combined NCD sample and preceding glue layer, were used to determined the average shock velocity in the NCD ($\langle U_{\text{s}}^{\text{NCD}} \rangle$). $\langle U_{\text{s}}^{\text{NCD}} \rangle$ was corrected using the method described in Sec. IV C to determine $U_{\text{s}}^{\text{NCD}}(t_1)$ at the IM interface. The shock velocity in the quartz [$U_{\text{s}}^{\text{Q}}(t_1)$] and $U_{\text{s}}^{\text{NCD}}(t_1)$ were used in the IM analysis to determine the particle velocity ($u_{\text{p}}^{\text{NCD}}$), pressure ($P^{\text{NCD}}$), and density ($\rho^{\text{NCD}}$) on the NCD Hugoniot. Shot numbers with an asterisk used liquid D_2–filled targets and were not included in the NCD Hugoniot fit because of the large uncertainty in measuring Δt_{total} from the lack of step/vacuum interfaces and glue-layer contractions in the cryogenic cells.

Shot	Δt_{total} (ns)	Δx_{total} (μm)	Δx_{NCD} (μm)	$\langle U_{\text{s}}^{\text{NCD}} \rangle$ (km/s)	$U_{\text{s}}^{\text{Q}}(t_1)$ (km/s)	$U_{\text{s}}^{\text{NCD}}(t_1)$ (km/s)	$u_{\text{p}}^{\text{NCD}}$ (km/s)	P^{NCD} (Mbar)	ρ^{NCD} (g cm^{-3})
77001	2.063 ± 0.020	64.24 ± 0.44	63.29 ± 0.45	31.10 ± 0.36	29.55 ± 0.09	31.25 ± 0.36	17.62 ± 0.13	18.50 ± 0.17	7.70 ± 0.17
77002	1.900 ± 0.023	62.27 ± 0.38	61.89 ± 0.29	32.75 ± 0.45	31.65 ± 0.09	33.02 ± 0.43	19.29 ± 0.16	21.40 ± 0.22	8.08 ± 0.22
77004*	2.384 ± 0.069	64.80 ± 0.54	64.97 ± 0.50	27.18 ± 0.82	25.94 ± 0.09	27.78 ± 0.81	14.85 ± 0.18	13.86 ± 0.26	7.22 ± 0.34
77005	2.092 ± 0.020	63.03 ± 0.31	62.69 ± 0.28	30.10 ± 0.33	30.19 ± 0.09	31.26 ± 0.31	18.24 ± 0.13	19.16 ± 0.16	8.07 ± 0.17
77006*	2.077 ± 0.063	64.19 ± 0.23	63.31 ± 0.50	30.87 ± 0.96	29.27 ± 0.09	31.18 ± 0.95	17.36 ± 0.23	18.19 ± 0.36	7.58 ± 0.41
77007	2.109 ± 0.019	63.44 ± 0.39	63.71 ± 0.33	30.08 ± 0.32	29.82 ± 0.09	31.28 ± 0.30	17.88 ± 0.12	18.79 ± 0.16	7.84 ± 0.15
77861	2.277 ± 0.021	63.06 ± 0.43	62.61 ± 0.30	27.67 ± 0.31	27.48 ± 0.09	28.89 ± 0.29	16.11 ± 0.11	15.64 ± 0.13	7.60 ± 0.14
77862	2.329 ± 0.019	61.72 ± 0.30	61.43 ± 0.27	26.49 ± 0.25	26.52 ± 0.09	27.67 ± 0.23	15.43 ± 0.10	14.35 ± 0.11	7.60 ± 0.12
79048	2.706 ± 0.011	62.18 ± 0.41	62.14 ± 0.27	22.98 ± 0.17	23.59 ± 0.17	24.54 ± 0.17	13.28 ± 0.16	10.95 ± 0.15	7.32 ± 0.12
79049	1.951 ± 0.008	62.07 ± 0.48	62.17 ± 0.26	31.81 ± 0.26	33.88 ± 0.16	35.10 ± 0.26	20.99 ± 0.22	24.76 ± 0.27	8.36 ± 0.18
79051	2.502 ± 0.011	62.65 ± 0.58	63.00 ± 0.25	25.04 ± 0.25	26.07 ± 0.16	27.60 ± 0.24	15.01 ± 0.16	13.92 ± 0.16	7.37 ± 0.14
79052	2.556 ± 0.011	63.58 ± 0.30	62.45 ± 0.34	24.81 ± 0.15	25.61 ± 0.16	27.08 ± 0.15	14.68 ± 0.16	13.36 ± 0.15	7.34 ± 0.11
79054	2.481 ± 0.011	61.31 ± 0.73	61.83 ± 0.28	24.71 ± 0.31	26.80 ± 0.16	27.16 ± 0.31	15.81 ± 0.17	14.43 ± 0.18	8.04 ± 0.21
79055	2.268 ± 0.010	61.54 ± 0.68	61.39 ± 0.25	27.12 ± 0.30	28.23 ± 0.16	29.71 ± 0.31	16.66 ± 0.17	16.63 ± 0.19	7.65 ± 0.17
79056	2.400 ± 0.008	65.17 ± 0.66	62.45 ± 0.30	26.97 ± 0.26	28.03 ± 0.16	29.53 ± 0.28	16.51 ± 0.17	16.38 ± 0.19	7.62 ± 0.15
79057	2.208 ± 0.010	61.60 ± 0.44	61.22 ± 0.25	27.87 ± 0.22	28.59 ± 0.16	29.94 ± 0.22	16.96 ± 0.17	17.06 ± 0.18	7.75 ± 0.14
79058	2.142 ± 0.015	62.72 ± 0.36	62.87 ± 0.25	29.28 ± 0.26	31.03 ± 0.16	32.42 ± 0.25	18.81 ± 0.18	20.49 ± 0.21	8.00 ± 0.16
79059	2.398 ± 0.010	61.66 ± 0.46	61.84 ± 0.25	25.71 ± 0.21	26.90 ± 0.16	28.41 ± 0.21	15.65 ± 0.16	14.94 ± 0.16	7.48 ± 0.13
79060	2.571 ± 0.015	61.89 ± 0.32	62.16 ± 0.42	24.07 ± 0.18	25.49 ± 0.16	26.74 ± 0.22	14.64 ± 0.17	13.15 ± 0.13	7.43 ± 0.16
21233 (EP)	1.931 ± 0.011	61.95 ± 0.41	61.40 ± 0.33	32.03 ± 0.26	33.99 ± 0.16	35.29 ± 0.25	21.05 ± 0.22	24.96 ± 0.27	8.33 ± 0.17
21237 (EP)	2.090 ± 0.010	63.02 ± 0.48	62.63 ± 0.26	30.12 ± 0.25	31.83 ± 0.16	33.43 ± 0.25	19.37 ± 0.19	21.75 ± 0.23	7.99 ± 0.15

combining these measurements with the thickness profiles of the individual samples (Δx_{NCD}), measured using a dual confocal microscope. Glue layers were kept to ~ 1 μm and are defined by $\Delta x_{\text{glue}} = \Delta x_{\text{total}} - \Delta x_{\text{NCD}}$. For some targets, Δx_{glue} was set to 0 μm because a negative glue thicknesses was inferred; the uncertainty always permitted a positive glue thickness. The average shock velocity in NCD alone was determined using $\langle U_{\text{s}}^{\text{NCD}} \rangle = (\Delta x_{\text{total}} - \Delta x_{\text{glue}})/\Delta t_{\text{NCD}}$.

C. Nonsteady waves correction

In laser-driven experiments, steady shocks are difficult to attain because of the expanding ablation plasma. A technique for correcting the average shock velocity to account for nonsteadiness was developed for use in laser-driven experiments [36]. For a large planar drive, the shock velocity history in an opaque sample is related to and corrected by the observed history in an adjacent transparent witness [36]. This requires that the EOS of the witness be known.

The amplitudes and temporal spacing of perturbations originating at the laser drive and arriving at the shock fronts in the NCD and the adjacent quartz witness depend on their relative equations of state. Deviations from $\langle U_{\text{s}}^{\text{NCD}} \rangle$ are correlated to the observed velocity history in the witness by $\delta U_{\text{s}}^{\text{NCD}}(t - t_1) = G \delta U_{\text{s}}^{\text{Q}}[(t - t_1)/F]$, where G and F are linear scaling factors that describe the relative amplitude and time history, respectively, of the shock-velocity profiles; $\delta U_{\text{s}}^{\text{Q}}$ is the deviation from the average shock velocity in the quartz witness over the time period $\Delta t_{\text{NCD}}/F$, which corresponds to the same set of temporal perturbations experienced by the NCD; F is determined by the relative sound speeds and Hugoniots in the two materials; and G is additionally affected by the Grüneisen parameters. The quartz Hugoniot and $\Gamma = \Gamma_{\text{eff}}(U_{\text{s}}^{\text{Q}})$ were taken from Ref. [26] and quartz sound speeds were determined from the derivatives of the release paths calculated using that construct. Since the intention of this work is to measure the NCD Hugoniot, an iterative process was used where initial estimates for the Hugoniot, Γ's, and sound speeds were taken from a tabular EOS (LEOS 9061) based on DFT-MD [24]. This EOS model was chosen because the high-pressure SCD Hugoniot data best agree with LEOS 9061 predictions. The NCD velocity histories for the entire data set were first determined using the correction with these initial estimates. Then, impedance matching was done using the measured U_{s}^{Q} and inferred $U_{\text{s}}^{\text{NCD}}$ at the IM interface to produce a linear $U_{\text{s}} - u_{\text{p}}$ relation for NCD. The process was repeated using the updated Hugoniot fit so that the NCD velocity profiles were iteratively corrected until the linear $U_{\text{s}} - u_{\text{p}}$ relation converged. An example of an NCD velocity history determined using this method is shown by the black curve in Fig. 1(c).

Velocity extrapolation across the glue layer at the quartz/NCD interface was treated differently to take advantage of the quartz witness. A continuous velocity profile was inferred across the glue layer at the quartz pusher/witness interface. Using this interpolation, the velocity profile in the

TABLE IV. ⟨110⟩ SCD Hugoniot data from impedance matching with a quartz standard.

Shot	U_s^Q (km/s)	U_s^{SCD} (km/s)	u_p^{SCD} (km/s)	P^{SCD} (Mbar)	ρ^{SCD} (g cm^{-3})
79050	27.54 ± 0.16	28.47 ± 0.10	15.98 ± 0.16	16.00 ± 0.16	8.02 ± 0.11
79053	28.68 ± 0.16	29.56 ± 0.10	16.85 ± 0.16	17.51 ± 0.17	8.17 ± 0.12
77848	32.94 ± 0.11	33.84 ± 0.06	20.00 ± 0.16	23.79 ± 0.19	8.59 ± 0.10
77858	33.17 ± 0.09	34.07 ± 0.06	20.16 ± 0.15	24.15 ± 0.18	8.61 ± 0.10
77860	33.77 ± 0.10	34.24 ± 0.06	20.70 ± 0.17	24.92 ± 0.20	8.89 ± 0.11
77851	34.62 ± 0.09	35.06 ± 0.06	21.32 ± 0.19	26.27 ± 0.24	8.97 ± 0.13
77856	34.82 ± 0.09	35.29 ± 0.07	21.46 ± 0.20	26.62 ± 0.25	8.97 ± 0.14

witness beginning at the time the shock enters the NCD ($t_1 + \Delta x_{glue}/U_s^{glue}$) is used in the nonsteady waves correction to determine F and G. With knowledge of F and G, $U_s^{NCD}(t) = \langle U_s^{NCD}\rangle + G\delta U_s^Q[(t - t_1)/F]$ is used to calculate the NCD shock velocities at times t_1 and t_2 needed for impedance matching.

V. RESULTS

This study of the Hugoniot and off-Hugoniot behaviors of two types of diamond was suitable for extracting the Grüneisen parameter for carbon. Γ of ∼1 for fluid carbon was determined by relating the experimentally measured NCD and SCD Hugoniots through a porosity model. This value was then confirmed by reproducing the NCD and SCD release data using Mie-Grüneisen EOS models that used the same Γ. A derivation of $\Gamma(\rho)$ is also presented.

A. Hugoniot data

1. SCD

The SCD Hugoniot data are listed in Table IV and plotted in Fig. 3 with existing data by Hicks *et al.* [14] and Knudson, Desjarlais, and Dolan [8]. The Hicks *et al.* experiments and this work, both IM experiments carried out using the OMEGA laser, used ⟨110⟩-oriented SCD and a quartz reference. The Knudson *et al.* experiments primarily used full-density (3.515 g cm^{-3}) microcrystalline diamond and were performed using magnetically driven flyer plate techniques. The existing data in Fig. 3 suggests that *SESAME* 7830 best models the Hugoniot across the coexistence region (6 to 10.5 Mbar) and beyond the melt. This work measured less compressibility, however, than *SESAME* 7830 above 16 Mbar; this stiffer behavior is predicted by a DFT-MD EOS model for multiphase carbon (LEOS 9061) [24].

The Hicks *et al.* data plotted in Fig. 3 are not the same as presented in the original publication; the data were reanalyzed using the updated quartz Hugoniot and the same reshock formulation presented here. For a given pressure, this re-analysis decreased the density by ∼3%.

For $P^C > 20$ Mbar (corresponding to $P^Q > 16$ Mbar at the IM point), the quartz Hugoniot fit used in impedance matching was extrapolated to higher pressures than given in the quartz data set [25,26]. If the extrapolation of the quartz Hugoniot is not valid at higher pressure, this could contribute to the apparent stiffening of the Hugoniot data that relied on a quartz standard.

2. NCD

The NCD Hugoniot was measured between 11 and 25 Mbar. The data are presented in Table III and plotted in the $U_s - u_p$ and $P - \rho$ planes in Fig. 4. The NCD $U_s - u_p$ Hugoniot data are approximately linear and were fit to $U_s = a_0 + a_1(u_p - \beta)$, where the coefficients and their standard deviations are listed in Table V. An orthogonally weighted least-squares linear fit was taken about the centroid of the data (β) so that the uncertainties in a_0 and a_1 are uncorrelated [44]. The standard deviation in the fit is given by $\sigma_{U_s}(u_p) = [\sigma_{a_0}^2 + \sigma_{a_1}^2(u_p - \beta)^2]^{1/2}$ [44].

The NCD data are slightly stiffer than predictions using LEOS 9061 [Fig. 4(b)], which well-represented the SCD Hugoniot in the same pressure range (Fig. 3). NCD's lower initial density ($m = \rho_0^{SCD}/\rho_0^{NCD} = 1.046$) and reduced

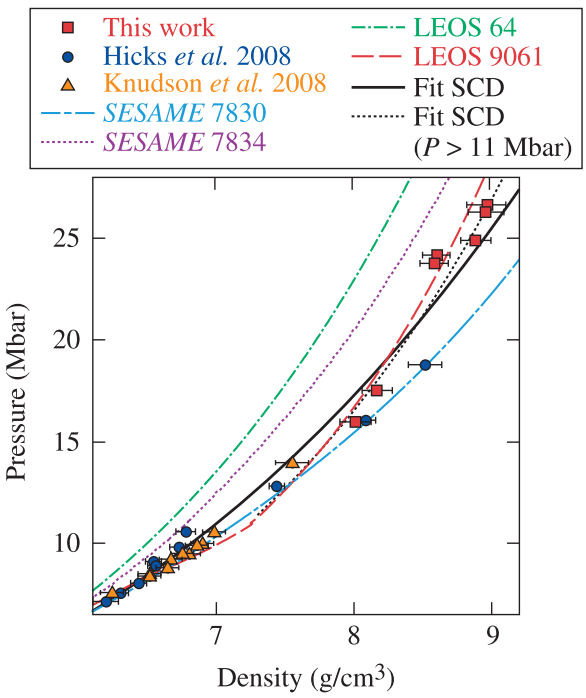

FIG. 3. Full-density ($\rho_0 = 3.515$ g cm^{-3}) diamond Hugoniot data. SCD data from this work (red squares), SCD data from Hicks *et al.* [14] re-analyzed using the updated quartz EOS [26] (blue circles), and polycrystalline data from Knudson, Desjarlais, and Dolan [8] (orange triangles). The data are compared to Hugoniots modeled using diamond EOS tables (colored curves). Weighted linear fits to the $U_s - u_p$ SCD data (this work and Hicks *et al.* [14]) projected into the $P - \rho$ plane (black curves).

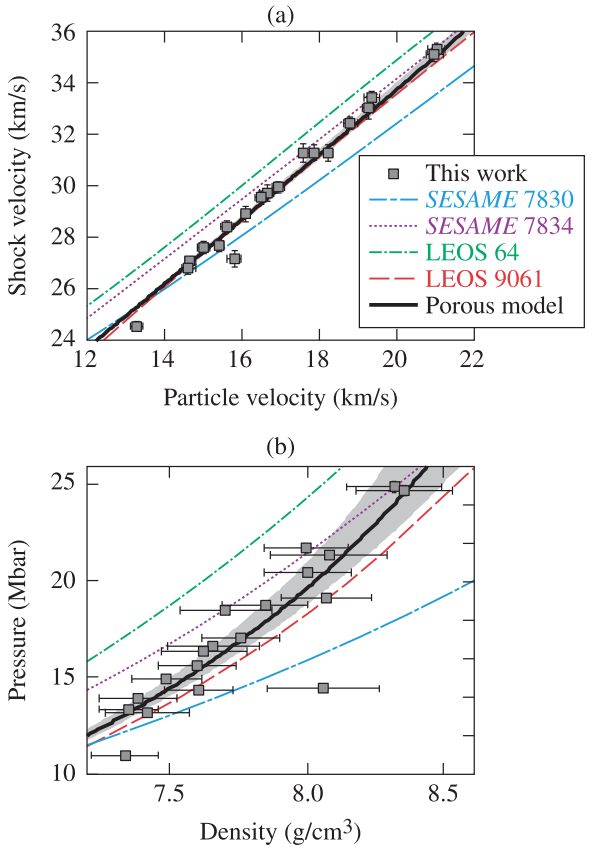

FIG. 4. NCD ($\rho_0 = 3.36\,\mathrm{g/cm^3}$) Hugoniot data (gray squares) from impedance matching with a quartz standard. (a) The shock velocity versus particle velocity data and (b) the pressure versus density data are compared to Hugoniots modeled using diamond EOS tables (colored curves) and a porous model (solid black curve) modeled using Eq.(8) with $\Gamma = 1.04$. The porous model using $\Gamma = 1.04 \pm 0.1$ is shown by gray-shaded areas. The Hugoniot curves derived from the EOS tables were modeled using the initial density of $3.36\,\mathrm{g\,cm^{-3}}$.

compressibility compared to SCD are consistent with that of a porous sample. Porous samples exhibit stiffer and even "reverse" Hugoniots as a result of added entropy during the pore-collapse phase of compression [23].

3. *Error analysis*

The values and errors in the Hugoniot data (Tables IV and III) represent the mean and standard deviation of each parameter determined using a Monte Carlo error analysis with 10 000 runs for NCD and 100 000 runs for SCD. For each run, the observable parameters (U_s^Q and U_s^{SCD} for SCD, or U_s^Q, Δx_{NCD}, Δx_{total}, Δt_{total}, and ρ_0^{NCD} for NCD) were varied within their error estimates. The cubic quartz $U_s - u_p$ coefficients and Γ_{eff} used in impedance matching were varied once per run using the covariance matrices listed in Ref. [26]. For NCD, the nonsteady waves correction and impedance matching were done each time until convergence was met, yielding 10 000 possible sets of Hugoniot data. The total error bars in ρ^{NCD} are between 1.5% and 3%, with the dominating error caused by the uncertainty in the target metrology and transit times. This Monte Carlo error analysis was used to evaluate the uncertainties in the re-analysis of the Hicks *et al.* SCD data [14] and Barrios *et al.* CH data [27].

TABLE V. Coefficients and uncertainties to the orthogonally weighted least-squares fit to the NCD $U_s - u_p$ data of the form $U_s = a_0 + a_1(u_p - \beta)$.

a_0 (km s^{-1})	a_1	β (km s^{-1})	σ_{a_0} (km s^{-1})	σ_{a_1}
29.416	1.356	16.59	0.077	0.037

B. The Grüneisen parameter

Differences between the SCD and NCD Hugoniots were used to determine the Grüneisen parameter for fluid carbon. We find that NCD's Hugoniot can be described by a simple porosity model from McQueen [22] (black curve in Fig. 4), given by

$$P_H^{NCD}(\rho) = P_H^{SCD}(\rho)\frac{1 - \frac{\Gamma}{2}\left(\frac{\rho}{\rho_0^{SCD}} - 1\right)}{1 - \frac{\Gamma}{2}\left(\frac{\rho}{\rho_0^{NCD}} - 1\right)}, \tag{8}$$

where P_H^{SCD} is the SCD Hugoniot, $\rho_0^{SCD} = 3.515\ \mathrm{g\,cm^{-3}}$, $\rho_0^{NCD} = 3.36\ \mathrm{g\,cm^{-3}}$, and $\Gamma = 1.04$. This model is derived from the definition of the Grüneisen parameter, such that the Hugoniots of the porous and crystal-density materials are related through Γ and their initial densities. The reference Hugoniot (P_H^{SCD}) was established by linearly fitting the SCD $U_s - u_p$ data in the same high-pressure fluid region (>11 Mbar) as where the NCD data were obtained. This orthogonally weighted linear fit is given by $U_s = (30.018 \pm 0.057) + (1.208 \pm 0.020)(u_p - 17.12)$ and shown in terms of $P - \rho$ by the dotted black curve in Fig. 3. For simplicity, Γ was assumed to be constant and was optimized at 1.04 to minimize the differences between the porous model and NCD Hugoniot data. The range of the porous model using $\Gamma = 1.04 \pm 0.1$ is represented by the gray-shaded area in Fig. 4.

A density-dependent Γ for liquid carbon was determined using the definition of the Grüneisen parameter and the two diamond Hugoniot fits. Both the SCD and NCD were shock compressed to a carbon fluid, however, the pressure and internal energy on the Hugoniots differ for a given density. These differences are used to estimate $\Gamma(\rho)$ using the definition $\Gamma \approx (1/\rho)(\Delta P/\Delta E)_\rho$, where $\Delta P = P_H^{NCD} - P_H^{SCD}$ and $\Delta E = E_H^{NCD} - E_H^{SCD}$ are evaluated at constant density. The linear $U_s - u_p$ fits projected onto the $P - \rho$ plane for NCD (Table V) and SCD (presented in the previous paragraph) are shown together in Fig. 5(a). These fits were used to solve for $\Gamma(\rho)$ [Fig. 5(b)].

$\Gamma(\rho)$ from this derivation is higher than predicted by the EOS tables above 7.5 $\mathrm{g\,cm^{-3}}$ [Fig. 5(b)]. $\Gamma \approx 1$ is ~20% higher than predicted by the DFT-MD model (red), which predicts $\Gamma \approx 0.8$ over the same density range as the data. This suggests that compared to the DFT-MD model, more energy goes into ΔP than other degrees of freedom for a given ΔE. This difference is related to the discrepancy between the DFT-MD Hugoniot (using ρ_0^{NCD}) and the NCD data despite agreement with the SCD Hugoniot data. Below 7.5 $\mathrm{g\,cm^{-3}}$ near the melt boundary (P ~10.5 Mbar), both $\Gamma(\rho)$ from this

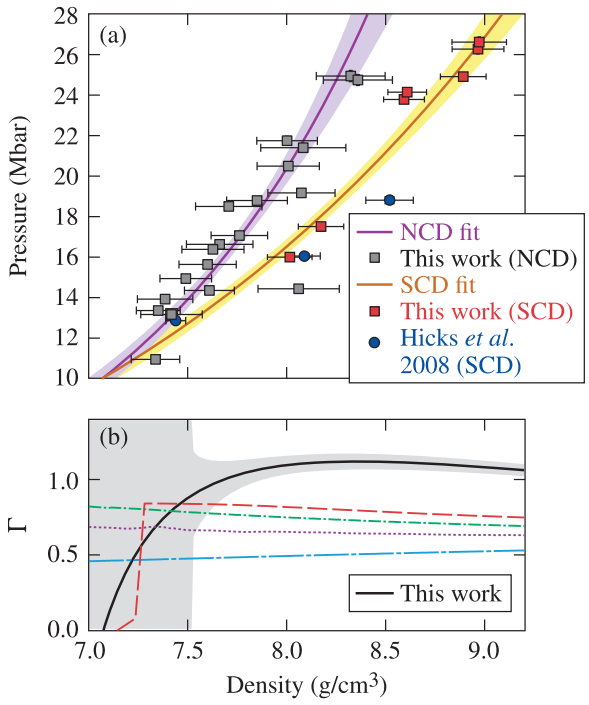

FIG. 5. (a) The NCD and SCD Hugoniot fits were used to derive (b) the Grüneisen parameter for liquid carbon. The density-dependent Γ from this work is higher than predictions using LEOS 9061 (dashed red curve), LEOS 64 (dashed–dotted green curve), SESAME 7834 (dotted purple curve), and SESAME 7830 (dashed–dotted blue curve). The shaded areas correspond to 1σ-uncertainty bands in the (a) NCD (purple) and SCD (yellow) fits and (b) $\Gamma(\rho)$ (gray).

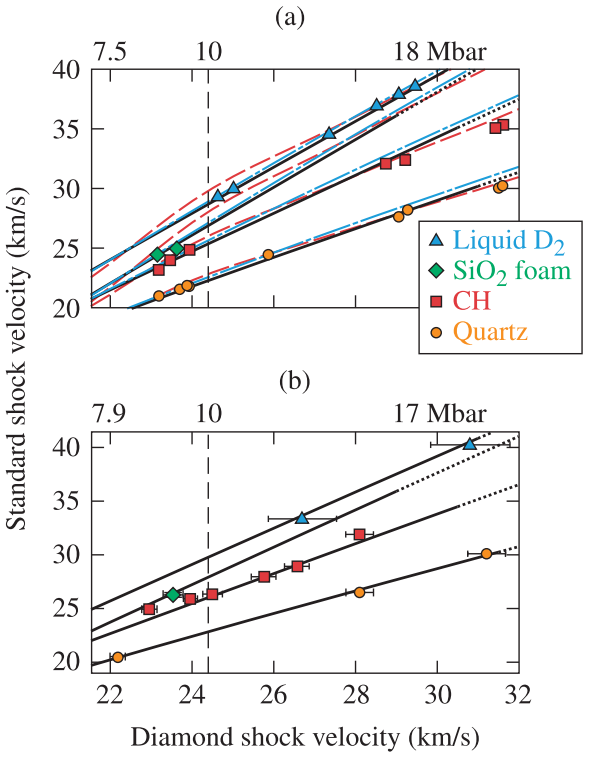

FIG. 6. (a) SCD and (b) NCD release data compared to predictions using diamond EOS models and existing Hugoniot fits for the standards. Data points are shock velocities for diamond releasing into liquid D_2 (blue triangles), SiO_2 foam (green diamonds), CH (red squares), and quartz (orange circles). Curves are the predicted $U_s^C - U_s^{Stan.}$ relationships determined using LEOS 9061 (dashed red), *SESAME* 7830 (dashed-dotted blue), and Mie-Grüneisen equations of state (solid black) to model the diamond Hugoniot and release paths and existing Hugoniot fits for the standards: liquid D_2 [29,30], SiO_2 foam [26,28], CH [27], and quartz [25,26]. Dotted portions of curves indicate that an extrapolation of the Hugoniot fit outside the standard's data range was used. The Mie-Grüneisen models for diamond used $\Gamma = 1.04$ and referenced a fit to the Hugoniot data from this work and Hicks *et al.* [14] for SCD (a) and the porous model for NCD (b). The top axes in (a) and (b) show the pressures on the Hugoniots used in the Mie-Grüneisen models that correspond to the diamond shock velocities on the bottom axes. The dashed vertical lines in (a) and (b) indicate the completion of melt on the SCD Hugoniot at 24.4(±0.4) km s^{-1} [7]. For data to the left of the line, diamond released from the coexistence region. For data to the right of the line, diamond released from the liquid phase. Error bars in (a) are about the size of the markers.

work and DFT-MD decrease towards zero. This is expected at a phase transition where there is a spike in the specific heat capacity ($\Gamma \propto 1/C_V$) [7]. However, the NCD and SCD data sets overlap over only 7.4 to 8.4 g cm^{-3} so our determination of $\Gamma(\rho)$ may only be valid over that density range. For this reason and because of the large uncertainty in $\Gamma(\rho)$ (determined from the 1σ uncertainties in the Hugoniot fits) below 7.5 g cm^{-3}, the constant $\Gamma = 1.04$ was used to evaluate the release data.

It has been shown for a number of systems that an increase in coordination can give rise to an increase in Γ [45–48]. One interpretation for our larger value of $\Gamma \approx 1$ in the liquid carbon compared to ambient diamond [$\Gamma = 0.85$ (Ref. [49])] and an ideal gas ($\Gamma = 2/3$) is an increase in coordination. This suggests that the dense carbon liquid is partially bonded at these conditions ($12 < P < 26$ Mbar on the Hugoniot).

C. Release data

The diamond release data (Table II) are plotted in Fig. 6 in terms of the observables, i.e., shock velocities on either side of the IM interface. The U_s^C and U_s^{Stan} data are shown for the release of diamond into quartz, CH, foam, and liquid D_2 (the orange circles, red squares, green diamonds, and blue triangles, respectively). The data are compared to the velocities predicted at the IM interface (curves) using diamond EOS models and the Hugoniots of the standards. These curves were created using states on the diamond Hugoniot (absissa) from which release paths were calculated. The intersections of the release paths with the known Hugoniot of the standard in the $P - u_p$ plane provided the final states (ordinate).

The SCD release data in Fig. 6(a) show that *SESAME* 7830 (dashed-dotted blue curves) and LEOS 9061 (dashed red curves) are best for modeling the diamond release in the pressure regimes where their respective Hugoniots are most valid, i.e., LEOS 9061 for $U_s^C > 28$ km/s and *SESAME* 7830 below that velocity. The SCD should be in the coexistence region upon release when $U_s^C < 24.4$ km/s, which corresponds to the completion of melt along the Hugoniot [7]. The data do not deviate from the *SESAME* 7830 predictions, which do not

include strength effects, indicating that strength does not play a significant role in the release from >8 Mbar. Shock wave splitting into an elastic precursor and inelastic wave should not occur until U_s^C decays below ∼22.3 km/s in ⟨110⟩ SCD and ∼21.6 km/s in polycrystalline diamond [17] and therefore should not affect the SCD or NCD data sets.

There is a ∼3% discrepancy between the DFT-MD (LEOS 9061) prediction and the two data points of SCD releasing into liquid D_2 from just above the melt boundary [Fig. 6(a)]. According to the DFT-MD calculations, the release paths originate in the liquid phase near 11 Mbar but cross into solid diamond upon release to ∼1.2 Mbar into the liquid D_2. The reduced shock velocity in the liquid D_2 compared to the predictions could indicate strength upon release since hydrostatic release isentropes were used to create the curves. However, if the DFT-MD Hugoniot is incorrect near 11–12 Mbar, that would cause a discrepancy. Figure 3 shows the lack of SCD Hugoniot data in that pressure range; the *SESAME* 7830 Hugoniot may be more accurate there. Indeed, the *SESAME* 7830 predictions agree very well with the two lowest pressure SCD-liquid D_2 points. For comparison, the Kerley deuterium model [50] predicts faster shock velocities at the IM interface than the Hicks Hugoniot fit used in this analysis. Overall, neither *SESAME* 7830 nor LEOS 9061 accurately describe all of the Hugoniot and release data.

In contrast to the tabular EOS models, a Mie-Grüneisen release model using the constant $\Gamma = 1.04$ (solid black curves) describes the entire data set. Since the release data span a wide range of pressures, this analytical model referenced a linear fit to all the SCD data from this work and Hicks *et al.* [14] given by $U_s = (26.449 \pm 0.036) + (1.105 \pm 0.010)(u_p - 13.75)$. This fit projected into the $P - \rho$ plane is shown by the solid black curve in Fig. 3. There is a discrepancy between the model and the highest pressure data in Fig. 6. However, the model provides a reasonable average between *SESAME* 7830 and LEOS 9061 in that region while still capturing the SCD behavior when releasing from lower pressures. This suggests that $\Gamma = 1.04$, which was derived for 11 Mbar $< P <$ 25 Mbar, may also be valid below 11 Mbar. IM experiments with a SCD standard can use this analytical release model to measure the Hugoniot of a lower impedance sample. SCD's transparancy is an added benefit because it leads to higher precision measurements.

The NCD data [Fig. 6(b)] are well-represented using a Mie-Grüneisen release model referencing the porous Hugoniot shown in Fig. 4 with $\Gamma = 1.04$ along the release path. The agreement between the analytical release models and the data for both NCD and SCD provide further confidence in $\Gamma = 1.04$. The NCD was most likely shocked into the liquid phase at the front NCD surface where the Hugoniot was measured. In the shots to the left of the melt line in Fig. 6(b), the shock decayed sufficiently during its transit that the NCD was at least partially solid upon release at its rear surface. This was apparent from the VISAR data of the unobstructed NCD step, which showed finite reflectivity at the NCD free surface after shock breakout, suggesting a solid rather than liquid state. The U_s^{Stan} data still follow the model's predictions even though the porous Hugoniot was fit to data only above the melt. These data cannot meaningfully be compared to the tabular EOS models because they do not accurately describe NCD's Hugoniot (Fig. 4), which determines the origin of the release path.

VI. CONCLUSIONS

The Hugoniot and release behavior of two types of diamond were measured at multimegabar pressures and the Grüneisen parameter for high-pressure fluid carbon was extracted from the experimental data sets. These measurements are important to constrain models used in planetary astrophysics and to design ICF targets with NCD ablators. The SCD Hugoniot above 15 Mbar agrees with DFT-MD calculations (LEOS 9061) in liquid carbon. NCD's response to shock compression is slightly stiffer than that of SCD and the DFT-MD predictions, even when accounting for its lower initial density. This behavior, which is described using a standard porosity model [22], should be included when modeling NCD's high-pressure behavior. This is important for ICF target designs, where the initial density of the NCD ablator can vary by a few percent based on the batch [13]. Another implication for ICF is that additional heating from the initial pore collapse affects NCD's high-pressure Hugoniot and raises the adiabat of the implosion.

We measured two data points of NCD releasing into liquid D_2 and six SCD/liquid D_2 data points, which are especially valuable for constraining ICF models that describe the NCD ablator release into the hydrogen fuel [31,32]. The diamond-liquid D_2 IM data can be reproduced when using the analytical release models and the experimental liquid-D_2 Hugoniot [29,30]. While *SESAME* 7830 and LEOS 9061 reproduce the SCD data over specific pressure ranges, none of the current EOS models capture the Hugoniot and release behaviors of both SCD and NCD. The analytical release models from this work can be used in IM experiments with SCD standards.

A Grüneisen parameter of 1.04 for liquid carbon was derived from the experimental NCD and SCD Hugoniots between 11 and 25 Mbar. Mie-Grüneisen EOS models using $\Gamma = 1.04$ accurately describe both the NCD and SCD experimental release data. This value of $\Gamma \approx 1$ is consistent over three independent analyses: (1) comparisons of the NCD and SCD Hugoniots, (2) the SCD, and (3) the NCD release analyses.

ACKNOWLEDGMENTS

This material is based upon work supported by the Department of Energy National Nuclear Security Administration under Award No. DE-NA0001944, the University of Rochester, and the New York State Energy Research and Development Authority. The support of DOE does not constitute an endorsement by DOE of the views expressed in this article. A portion of this work was conducted at Lawrence Livermore National Laboratory under Contract No. DE-AC52-07NA27344.

This report was prepared as an account of work sponsored by an agency of the U.S. Government. Neither the U.S. Government nor any agency thereof, nor any of their employees, makes any warranty, express or implied, or assumes any legal liability or responsibility for the accuracy, completeness, or usefulness of any information, apparatus, product, or

process disclosed, or represents that its use would not infringe privately owned rights. Reference herein to any specific commercial product, process, or service by trade name, trademark, manufacturer, or otherwise does not necessarily constitute or imply its endorsement, recommendation, or favoring by the U.S. Government or any agency thereof. The views and opinions of authors expressed herein do not necessarily state or reflect those of the U.S. Government or any agency thereof.

[1] M. Ross, Nature (London) **292**, 435 (1981).

[2] N. Madhusudhan, K. K. M. Lee, and O. Mousis, Astrophys. J. Lett. **759**, L40 (2012).

[3] H. Van Horn, *Unlocking the Secrets of White Dwarf Stars* (Springer International Publishing, Switzerland, 2015).

[4] T. S. Metcalfe, M. H. Montgomery, and A. Kanaan, Astrophys. J. Lett. **605**, L133 (2004).

[5] F. Ancilotto, G. L. Chiarotti, S. Scandolo, and E. Tosatti, Science **275**, 1288 (1997).

[6] T. Guillot, Annu. Rev. Earth Planet. Sci. **33**, 493 (2005).

[7] J. H. Eggert, D. G. Hicks, P. M. Celliers, D. K. Bradley, R. S. McWilliams, R. Jeanloz, J. E. Miller, T. R. Boehly, and G. W. Collins, Nat. Phys. **6**, 40 (2010).

[8] M. D. Knudson, M. P. Desjarlais, and D. H. Dolan, Science **322**, 1822 (2008).

[9] A. A. Correa, L. X. Benedict, D. A. Young, E. Schwegler, and S. A. Bonev, Phys. Rev. B **78**, 024101 (2008).

[10] A. J. MacKinnon, N. B. Meezan, J. S. Ross, S. Le Pape, L. Berzak Hopkins, L. Divol, D. Ho, J. Milovich, A. Pak, J. Ralph *et al.*, Phys. Plasmas **21**, 056318 (2014).

[11] J. S. Ross, D. Ho, J. Milovich, T. Döppner, J. McNaney, A. G. MacPhee, A. Hamza, J. Biener, H. F. Robey, E. L. Dewald, R. Tommasini, L. Divol, S. Le Pape, L. B. Hopkins, P. M. Celliers, O. Landen, N. B. Meezan, and A. J. Mackinnon, Phys. Rev. E **91**, 021101 (2015).

[12] J. Biener, D. D. Ho, C. Wild, E. Woerner, M. M. Biener, B. S. El-dasher, D. G. Hicks, J. H. Eggert, P. M. Celliers, G. W. Collins, N. E. Teslich, Jr., B. J. Kozioziemski, S. W. Haan, and A. V. Hamza, Nucl. Fusion **49**, 112001 (2009).

[13] C. Dawedeit, S. O. Kucheyev, S. J. Shin, T. M. Willey, M. Bagge-Hansen, T. Braun, Y. M. Wang, B. S. El-Dasher, N. E. Teslich, M. M. Biener, J. Ye, L. Kirste, C.-C. Roehlig, M. Wolfer, E. Woerner, A. W. van Buuren, A. V. Hamza, C. Wild, and J. Biener, Diam. Relat. Mater. **40**, 75 (2013).

[14] D. G. Hicks, T. R. Boehly, P. M. Celliers, D. K. Bradley, J. H. Eggert, R. S. McWilliams, R. Jeanloz, and G. W. Collins, Phys. Rev. B **78**, 174102 (2008).

[15] H. Nagao, K. G. Nakamura, K. Kondo, N. Ozaki, K. Takamatsu, T. Ono, T. Shiota, D. Ichinose, K. A. Tanaka, K. Wakabayashi, K. Okada, M. Yoshida, M. Nakai, K. Nagai, K. Shigemori, T. Sakaiya, and K. Otani, Phys. Plasmas **13**, 052705 (2006).

[16] S. Brygoo, E. Henry, P. Loubeyre, J. Eggert, M. Koenig, B. Loupias, A. Benuzzi-Mounaix, and M. Rabec Le Gloahec, Nat. Mater. **6**, 274 (2007).

[17] R. S. McWilliams, J. H. Eggert, D. G. Hicks, D. K. Bradley, P. M. Celliers, D. K. Spaulding, T. R. Boehly, G. W. Collins, and R. Jeanloz, Phys. Rev. B **81**, 014111 (2010).

[18] K. Kondo and T. J. Ahrens, Geophys. Res. Lett. **10**, 281 (1983).

[19] M. N. Pavlovskii, Sov. Phys. Solid State **13**, 741 (1971).

[20] R. F. Smith, J. H. Eggert, R. Jeanloz, T. S. Duffy, D. G. Braun, J. R. Patterson, R. E. Rudd, J. Biener, A. E. Lazicki, A. V. Hamza, J. Wang, T. Braun, L. X. Benedict, P. M. Celliers, and G. W. Collins, Nature (London) **511**, 330 (2014).

[21] D. K. Bradley, J. H. Eggert, R. F. Smith, S. T. Prisbrey, D. G. Hicks, D. G. Braun, J. Biener, A. V. Hamza, R. E. Rudd, and G. W. Collins, Phys. Rev. Lett. **102**, 075503 (2009).

[22] R. G. McQueen, S. P. Marsh, J. W. Taylor, J. N. Fritz, and W. J. Carter, in *High-Velocity Impact Phenomena*, edited by R. Kinslow (Academic, New York, 1970).

[23] Y. B. Zel'dovich and Y. P. Raizer, *Physics of Shock Waves and High-Temperature Hydrodynamic Phenomena*, edited by W. D. Hayes and R. F. Probstein (Academic, New York, 1966).

[24] L. X. Benedict, K. P. Driver, S. Hamel, B. Militzer, T. Qi, A. A. Correa, A. Saul, and E. Schwegler, Phys. Rev. B **89**, 224109 (2014).

[25] M. D. Knudson and M. P. Desjarlais, Phys. Rev. Lett. **103**, 225501 (2009).

[26] M. D. Knudson and M. P. Desjarlais, Phys. Rev. B **88**, 184107 (2013).

[27] M. A. Barrios, D. G. Hicks, T. R. Boehly, D. E. Fratanduono, J. H. Eggert, P. M. Celliers, G. W. Collins, and D. D. Meyerhofer, Phys. Plasmas **17**, 056307 (2010).

[28] M. D. Knudson and R. W. Lemke, J. Appl. Phys. **114**, 053510 (2013).

[29] D. G. Hicks, T. R. Boehly, P. M. Celliers, J. H. Eggert, S. J. Moon, D. D. Meyerhofer, and G. W. Collins, Phys. Rev. B **79**, 014112 (2009).

[30] M. D. Knudson, M. P. Desjarlais, and A. Pribram-Jones, Phys. Rev. B **91**, 224105 (2015).

[31] H. F. Robey, T. R. Boehly, P. M. Celliers, J. H. Eggert, D. Hicks, R. F. Smith, R. Collins, M. W. Bowers, K. G. Krauter, P. S. Datte *et al.*, Phys. Plasmas **19**, 042706 (2012).

[32] S. Hamel, L. X. Benedict, P. M. Celliers, M. A. Barrios, T. R. Boehly, G. W. Collins, T. Döppner, J. H. Eggert, D. R. Farley, D. G. Hicks, J. L. Kline, A. Lazicki, S. LePape, A. J. Mackinnon, J. D. Moody, H. F. Robey, E. Schwegler, and P. A. Sterne, Phys. Rev. B **86**, 094113 (2012).

[33] T. R. Boehly, D. L. Brown, R. S. Craxton, R. L. Keck, J. P. Knauer, J. H. Kelly, T. J. Kessler, S. A. Kumpan, S. J. Loucks, S. A. Letzring, F. J. Marshall, R. L. McCrory, S. F. B. Morse, W. Seka, J. M. Soures, and C. P. Verdon, Opt. Commun. **133**, 495 (1997).

[34] S. Skupsky, R. W. Short, T. Kessler, R. S. Craxton, S. Letzring, and J. M. Soures, J. Appl. Phys. **66**, 3456 (1989).

[35] Y. Lin, T. J. Kessler, and G. N. Lawrence, Opt. Lett. **20**, 764 (1995).

[36] D. E. Fratanduono, D. H. Munro, P. M. Celliers, and G. W. Collins, J. Appl. Phys. **116**, 033517 (2014).

[37] E. I. Moses, R. N. Boyd, B. A. Remington, C. J. Keane, and R. Al-Ayat, Phys. Plasmas **16**, 041006 (2009).

[38] P. C. Souers, *Hydrogen Properties for Fusion Energy* (University of California Press, Berkeley, CA, 1986).

[39] P. M. Celliers, D. K. Bradley, G. W. Collins, D. G. Hicks, T. R. Boehly, and W. J. Armstrong, Rev. Sci. Instrum. **75**, 4916 (2004).
[40] M. C. Gregor, R. Boni, A. Sorce, J. Kendrick, C. A. McCoy, D. N. Polsin, T. R. Boehly, P. M. Celliers, G. W. Collins, D. E. Fratanduono, J. H. Eggert, and M. Millot, Rev. Sci. Instrum. **87**, 114903 (2016).
[41] G. R. Gathers, *Selected Topics in Shock Wave Physics and Equation of State Modeling* (World Scientific, New Jersey, 1994).
[42] M. M. Marinak, G. D. Kerbel, N. A. Gentile, O. Jones, D. Munro, S. Pollaine, T. R. Dittrich, and S. W. Haan, Phys. Plasmas **8**, 2275 (2001).
[43] A. Lazicki *et al.* (unpublished).
[44] P. M. Celliers, G. W. Collins, D. G. Hicks, and J. H. Eggert, J. Appl. Phys. **98**, 113529 (2005).
[45] A. K. Verma, P. Modak, and B. B. Karki, Phys. Rev. B **84**, 174116 (2011).
[46] L. Stixrude and B. Karki, Science **310**, 297 (2005).
[47] M. C. Roufosse and R. Jeanloz, J. Geophys. Res. **88**, 7399 (1983).
[48] T. H. K. Barron, Nature (London) **178**, 871 (1956).
[49] A. Dewaele, F. Datchi, P. Loubeyre, and M. Mezouar, Phys. Rev. B **77**, 094106 (2008).
[50] G. I. Kerley, Sandia National Laboratories Report No. SAND2003-3613, 2003.